

# Higher-Order Kuramoto Oscillator Network for Dense Associative Memory

Jona Nägerl<sup>1</sup> and Natalia G. Berloff<sup>1,\*</sup>

<sup>1</sup>*Department of Applied Mathematics and Theoretical Physics,  
University of Cambridge, Wilberforce Road, Cambridge CB3 0WA, United Kingdom*  
(Dated: July 30, 2025)

Networks of phase oscillators can serve as dense associative memories if they incorporate higher-order coupling beyond the classical Kuramoto model's pairwise interactions. Here we introduce a generalized Kuramoto model with combined second-harmonic (pairwise) and fourth-harmonic (quartic) coupling, inspired by dense Hopfield memory theory. Using mean-field theory and its dynamical approximation, we obtain a phase diagram for dense associative memory model that exhibits a tricritical point at which the continuous onset of memory retrieval is supplanted by a discontinuous, hysteretic transition. In the quartic-dominated regime, the system supports bistable phase-locked states corresponding to stored memory patterns, with a sizable energy barrier between memory and incoherent states. We analytically determine this bistable region and show that the escape time from a memory state (due to noise) grows exponentially with network size, indicating robust storage. Extending the theory to finite memory load, we show that higher-order couplings achieve superlinear scaling of memory capacity with system size, far exceeding the limit of pairwise-only oscillators. Large-scale simulations of the oscillator network confirm our theoretical predictions, demonstrating rapid pattern retrieval and robust storage of many phase patterns. These results bridge the Kuramoto synchronization with modern Hopfield memories, pointing toward experimental realization of high-capacity, analog associative memory in oscillator systems.

## INTRODUCTION

The ability of a dynamical system to store and robustly retrieve a large set of patterns commonly referred to as associative memory is a cornerstone of both theoretical neuroscience and neuromorphic computing. Since the seminal work of Hopfield [1], fully connected networks with binary spins and pairwise couplings have served as the canonical model, but they suffer from fundamental limitations: their storage capacity scales only linearly with the system size  $N$  and, beyond capacity, spurious minima proliferate in the energy landscape, degrading retrieval fidelity.

To overcome these limitations, dense associative memory (DAM) models introduce higher-order interactions into the energy landscape,

$$E(\sigma) = - \sum_{m=1}^p \frac{1}{m!} \sum_{i_1, \dots, i_m=1}^N J_{i_1 \dots i_m}^{(m)} \sigma_{i_1} \cdots \sigma_{i_m}, \quad (1)$$

where  $\sigma_i \in \{-1, +1\}$  are "spins",  $p$  is the highest interaction order retained and  $J_{i_1 \dots i_m}^{(m)}$  is the symmetric  $m$ -th-order coupling tensor. Adopting the Hebbian rule, the couplings are

$$J_{i_1 \dots i_m}^{(m)} = (1/P) \sum_{\mu=1}^P \xi_{i_1}^\mu \cdots \xi_{i_m}^\mu, \quad (2)$$

where  $\{\xi^\mu\}_{\mu=1}^P$  are the binary patterns to be stored. Mean-field analysis shows that DAMs with interaction order  $p \geq 3$  store an extensive number of uncorrelated patterns,  $P_{\max} = O(N^{p-1})$ , while energetically lifting spurious states [2, 3]. This model has smooth degrada-

tion at overload and forms a bridge to modern energy-based learning [4], in that the Hopfield energy with  $p \geq 3$  can emulate the loss function of a deep neural network with rectified units [2, 3].

Further, oscillatory networks offer a powerful analog alternative to binary associative memories storing patterns as stable phase-locked states of coupled oscillators. Their continuous dynamics can exploit graded synchronization levels and phase differences to encode information, offering a richer computational behavior. This makes oscillatory associative memories attractive for energy-efficient, in-memory computing applications where continuous variables and analog processing are advantageous.

The Kuramoto model, with its simple sinusoidal (first harmonic) coupling, provides a canonical framework for studying synchronization [5]. However, classical Kuramoto networks with only pairwise phase coupling (e.g.,  $J_{ij} \sin \phi_{ij}$  where  $\phi_{ij}$  stands for the phase difference between the oscillators  $i$  and  $j$ ) are insufficient for robust memory retrieval. Past analyses show they can store only a vanishing small number of patterns without error, on the order of a few, regardless of network size [6]. To address this problem second-harmonic terms are introduced into the coupling: a so-called resonant Kuramoto model that adds a  $\sin(2\phi_{ij})$  component. This second-order coupling stabilizes the phase-locked memory patterns and dramatically boosts the memory capacity and allows the network to store on the order of  $N/\log N$  patterns [6].

The resonant Kuramoto model and dense associative Hopfield networks motivate the exploration of higher-order interactions in oscillator networks. Recent work in physics and neuroscience has highlighted that beyond pairwise coupling three-body or four-body interactions

among units can fundamentally alter collective dynamics [7]. By generalizing beyond the second harmonic (pairwise) resonance to include  $p$ -body coupling terms, one can in principle combine the best of both worlds: the analog, phase-continuous inference of oscillatory systems and the high capacity of modern Hopfield networks. This motivates the exploration of oscillator networks with genuine three-body and four-body interactions, which have recently been shown to induce multistability, abrupt synchronization transitions, and richer dynamical regimes beyond pairwise coupling [8].

In this paper, we introduce a higher-order Kuramoto model for associative memory retrieval, incorporating many-body phase interactions. Specifically, we implement effective  $p = 4$  couplings in the phase dynamics—a choice motivated by dense memory theory, which shows that quartic interaction terms are essential for storing many patterns [3]. Crucially, we retain the quadratic coupling alongside the quartic term, reflecting both physical plausibility and enhanced computational stability. On the physical side, higher-order nonlinear couplings in real oscillatory systems are usually accompanied by lower-order harmonics; for instance, nonlinear oscillator platforms can naturally generate second-harmonic interactions (and by extension, combined multi-harmonic interactions) without sacrificing locality [9]. On the computational side, including the lower-order term enhances the robustness of retrieval dynamics: weak pairwise terms deepen the basins of attraction of stored patterns, reducing the critical noise required to trigger retrieval failure, as confirmed by both analytic overlap equations and time-domain simulations below. This higher-order Kuramoto network is still amenable to analysis but has a richer phase space structure capable of hosting many stable phase-locked configurations corresponding to stored memories.

Fourth-order phase coupling is no longer a purely theoretical construct; contemporary oscillator hardware can already engineer programmable coupling functions across analog and neuromorphic platforms, from optical to electronic oscillators [10, 11]. In photonics, a spatial light modulator can emulate the high-order interaction with frequency conversion in a nonlinear crystal [12], while nonlinear four-wave mixing in coupled laser arrays, fibers and metamaterials achieves a similar multi-oscillator entanglement [13–16]. Exciton-polariton condensate lattices can generate effective four-body interactions via nonlinear gain depletion [9, 17]. Many of these systems operate at GHz–THz bandwidths, so the resulting fourth-order Kuramoto dynamics unfolds on sub-nanosecond timescales. Electronic and quantum circuits are reaching similar capabilities. Superconducting Kerr-parametric-oscillator (KPO) arrays employ four-junction plaquette couplers that realize local quartic terms compatible with the Lechner-Hauke-Zoller mapping [18]. An alternative direction leverages higher-

order oscillator dynamics to solve combinatorial problems, as demonstrated in recent work on dynamical Ising machines for NAE-K-SAT and hypergraph Max-K-Cut, which implement fourth-order interactions via harmonic coupling in phase-based networks [19, 20]. Similar logic has also been realized in resistive TCAM-based accelerators such as KLIMA, which directly solve k-SAT problems by encoding higher-order clause evaluation in analog in-memory architectures, thereby further validating the feasibility of non-quadratic dynamical coupling schemes [21]. Recent work has shown that photonic spiking-neuron networks built from time-multiplexed degenerate optical parametric oscillators can host rich higher-order dynamics, including self-organized chimera states that emerge from adaptive phase coupling and spiking-mode shifts [22]. Recent spintronic implementations have also demonstrated higher-order phase interactions, such as second-harmonic injection locking in spin-torque nano-oscillators [23] and weighted spin-torque oscillators that integrate multiple synaptic inputs in a single nonlinear node [24–26]. Even in equilibrium condensed-matter physics, four-spin ring-exchange interactions are well established in certain quantum magnets [27], underscoring the ubiquity of genuine multi-body couplings. These observations confirm that the  $p = 4$  regime is experimentally accessible with current photonic, superconducting, and semiconductor technologies, paving the way for dense associative-memory prototypes.

The rest of the paper is arranged as follows: Firstly, we present the higher-order Kuramoto model and its interpretation in terms of equilibrium statistical mechanics. This includes a derivation of the static mean-field free energy and its Landau expansion, followed by a dynamical mean-field approximation. We then construct the saddle-node bifurcation line analytically. Next, we analyze escape times in the presence of noise via Kramer escape time theory, focusing on behavior near the tricritical line. We also extend mean-field theory to account for pattern interference in memory settings. After this, we perform large-scale numerical simulations to confirm the analytical results and to study memory retrieval. We detail the efficient simulation of higher-order dynamics, test the validity of mean-field predictions under varying memory load, and examine how capacity scales with network size.

## HIGHER-ORDER KURAMOTO MODELS

Networks of weakly-coupled limit-cycle oscillators represent a natural continuous-phase generalization of Hopfield dynamics [1]. Phases  $\theta_i \in [0, 2\pi)$  encode information continuously rather than discretely, and the collective evolution towards synchronized or phase-locked states implements an energy-minimization process analogous to gradient descent on a Lyapunov functional. Yet

the classical Kuramoto interaction,

$$\dot{\theta}_i = \omega_i + \frac{1}{N} \sum_{j=1}^N J_{ij} \sin(\theta_j - \theta_i), \quad (3)$$

where  $\omega_i$  are natural frequencies of the oscillators, retains only the first Fourier harmonic of the  $2\pi$ -periodic coupling kernel. This restriction confines the dynamical behavior to global synchrony or, at best, a small set of cluster states fixed by heterogeneity, whereas associative memory retrieval demands a multitude of coexisting stable phase-locked configurations [5, 28].

A minimal and experimentally accessible extension introduces the second harmonic term leading to

$$\dot{\theta}_i = \omega_i + \frac{1}{N} \sum_{j=1}^N J_{ij} \sin(\theta_j - \theta_i) + \frac{\epsilon}{N^2} \sum_{j=1}^N \sin 2(\theta_j - \theta_i), \quad (4)$$

commonly termed the second-resonance Kuramoto model [6]. Here  $\epsilon$  can scale up to  $\mathcal{O}(N)$ , ensuring the second-harmonic term contributes a finite effect as  $N \rightarrow \infty$ . The additional  $\sin 2\Delta\theta$  term creates a double-well effective potential, energetically favoring phase differences close to 0 or  $\pi$ . This binarization stabilizes discrete-valued phase patterns, suppresses marginal modes that plague the plain model, and thereby remedies its tendency toward drift and spurious asynchronous states.

Building on the DAM paradigm, we elevate Eq. (4) to a general  $p$ -body phase model whose Lyapunov functional contains both pairwise and higher-order cosine kernels,

$$\mathcal{H}(\boldsymbol{\theta}) = - \frac{1}{N} \sum_{i < j} J_{ij} \cos(\theta_i - \theta_j) - \frac{1}{N^{(p-1)}} \sum_{i_1 < \dots < i_p} K_{i_1 \dots i_p} \cos(\Delta\theta_{1 \dots p}), \quad (5)$$

where  $p$  is even,  $\Delta\theta_{1 \dots p} \equiv \theta_{i_1} + \dots + \theta_{i_{p/2}} - \theta_{i_{p/2+1}} - \dots - \theta_{i_p}$ , and  $K_{i_1 \dots i_p} \propto \sum_{\mu=1}^P \xi_{i_1}^\mu \dots \xi_{i_p}^\mu$  is a Hebbian imprint of  $P$  dense patterns [3]. The similarity of the state  $\boldsymbol{\theta}$  with the patterns are calculated by the overlaps  $r_\mu e^{i\phi_\mu} = N^{-1} \sum_j \xi_j^\mu e^{i\theta_j}$ .

In this paper we focus on the quartic ( $p = 4$ ) case, combining (i) a mean-field equilibrium analysis to estimate storage capacity and basin geometry, (ii) a dynamical stability study of the fixed points of the 4-body flow, and (iii) extensive numerical experiments that compare recall performance with and without the residual quadratic channel. This combined approach allows us to isolate the distinct roles played by two- and four-body interactions and to chart design guidelines for hardware realizations of high-capacity oscillatory memories [7, 29]. Recent theoretical work has also shown that the representation of higher-order interactions via hypergraphs versus simplicial complexes can lead to qualitatively distinct synchro-

nization dynamics, reinforcing the importance of carefully modeling the nature of  $p$ -body coupling [30].

We consider a population of  $N$  phase oscillators whose dynamics combine pairwise and four-body phase couplings ( $J - K$  Kuramoto model),

$$\dot{\theta}_i = \omega_i + \frac{J}{N} \sum_{j=1}^N J_{ij} \sin(\theta_j - \theta_i) + \frac{K}{6N^3} \sum_{j,k,\ell=1}^N K_{ijkl} \sin(\theta_j + \theta_k - \theta_\ell - \theta_i). \quad (6)$$

Here  $J$  is the overall strength of the pairwise (1-simplex) interaction. The accompanying matrix  $J_{ij}$  stores the binary patterns  $\{\xi_i^\mu\}_{\mu=1}^P \subset \{\pm 1\}^N$  with the usual Hebbian learning rule

$$J_{ij} = \frac{1}{P} \sum_{\mu=1}^P \xi_i^\mu \xi_j^\mu \quad (i \neq j), \quad (7)$$

so that the first summation in Eq. (6) coincides with the Hopfield coupling written in phase form ( $\xi = +1$  mapped to  $\theta = 0$ ,  $\xi = -1$  to  $\theta = \pi$ ).  $K$  is the overall strength of the four-body (3-simplex) interaction. The tensor  $K_{ijkl}$  encodes the same set of memories but now via a quartic Hebbian rule

$$K_{ijkl} = \frac{1}{P} \sum_{\mu=1}^P \xi_i^\mu \xi_j^\mu \xi_k^\mu \xi_\ell^\mu, \quad (8)$$

symmetric under any permutation of its indices. The factors  $1/N$  and  $1/N^3$  ensure that both interaction terms remain  $\mathcal{O}(1)$  as  $N \rightarrow \infty$ . Throughout this paper we use the notation so that  $J_{ij}$  and  $K_{ijkl}$  are pattern-derived coupling matrices/tensors, while  $J$  and  $K$  (without indices) control the overall interaction strength. The higher-order term is the phase analogue of the  $p = 4$  dense-Hopfield interaction [2]. Such quartic terms naturally arise in oscillator-based solvers for constraint optimization problems, where the logical structure of higher-order SAT clauses is mapped directly to phase-coupled networks using fourth-harmonic injection [20, 31]. The higher-order tensors were also experimentally demonstrated in FPGA-based implementations of probabilistic computing architectures for solving hard constraint problems natively formulated with higher-order logic [32].

### Equilibrium (Static) Mean-Field Free Energy

Near the attractor states, where after a binary gauge rotation the effective couplings  $J_{ij}$  and  $K_{ijkl}$  take approximately uniform values, i.e.,  $J_{ij}, K_{ijkl} \approx 1$ , the dynamics of Eq. (6) can be interpreted in the equilibrium limit as

a static  $XY$  spin model governed by an effective Hamiltonian

$$H = -\frac{J}{2N} \sum_{i,j} \cos(\theta_j - \theta_i) - \frac{K}{24N^3} \sum_{i,j,k,\ell} \cos(\theta_k + \theta_\ell - \theta_i - \theta_j), \quad (9)$$

with the order parameter  $z = \frac{1}{N} \sum_i e^{i\theta_i}$  so that  $r(t) = |z(t)| \in [0, 1]$  measures the degree of synchrony, and  $\psi(t) = \arg z(t)$  is the collective phase. In the mean-field approximation, each spin experiences the effective field  $Jr + \frac{K}{6}r^3$ . Following the standard Legendre construction one obtains (see e.g. [29] for  $k = 1, 2$ ) the free-energy density  $F(r) \equiv \beta f(r)$  as

$$F(r) = \frac{\beta J}{2} r^2 + \frac{\beta K}{8} r^4 - \ln[I_0(\beta(Jr + \frac{K}{6}r^3))], \quad (10)$$

where  $\beta = 1/k_B T$  and we let  $k_B = 1$ . The stationary state  $\partial f / \partial r = 0$  yields

$$r = \frac{I_1(\beta(Jr + \frac{K}{6}r^3))}{I_0(\beta(Jr + \frac{K}{6}r^3))}, \quad (11)$$

where  $I_0$  and  $I_1$  are the modified Bessel functions.

*Landau expansion of the free energy and location of the critical and tricritical points.* We expand the mean-field free energy  $f(r)$  in Eq. (10) in powers of the order parameter  $r$  around  $r = 0$  up to the sixth order, so that

$$f(r) = a_2 r^2 + a_4 r^4 + a_6 r^6 + O(r^8), \quad (12)$$

with

$$\begin{aligned} a_2 &= \frac{J}{2} \left(1 - \frac{\beta J}{2}\right), \\ a_4 &= \frac{J^4 \beta^3}{64} - \frac{JK\beta}{12} + \frac{K}{8}, \\ a_6 &= -\frac{J^6 \beta^5}{576} + \frac{J^3 K \beta^3}{96} - \frac{K^2 \beta}{144}. \end{aligned} \quad (13)$$

The coefficient  $a_2$  changes sign at  $a_2 = 0$ , so at  $x_P = \beta J = 2$ . For  $x > x_P$  the only minimum of  $f$  is the coherent non zero state  $r \neq 0$ . Whether this new minimum emerges continuously or discontinuously is governed by the sign of  $a_4$  evaluated on the critical line  $\beta J = 2$ . Substituting  $\beta = 2/J$  into  $a_4$  gives  $a_4(\beta J = 2) = J/8 - K/24$ . Hence, if  $K < 3J$  the quartic coefficient is positive;  $f(r)$  then has the standard ‘‘Mexican-hat’’ shape and the overlap grows as  $r \sim \sqrt{T_c - T}$ , i.e. the transition is second order.

*Tricritical point and first-order branch.* The quartic term vanishes when  $K = 3J$ , which marks a tricritical point  $(\beta_{\text{tri}}, K_{\text{tri}}) = (2/J, 3J)$ . For  $K > K_{\text{tri}}$  one has  $a_4 < 0$ : the quartic term alone would bend the Landau

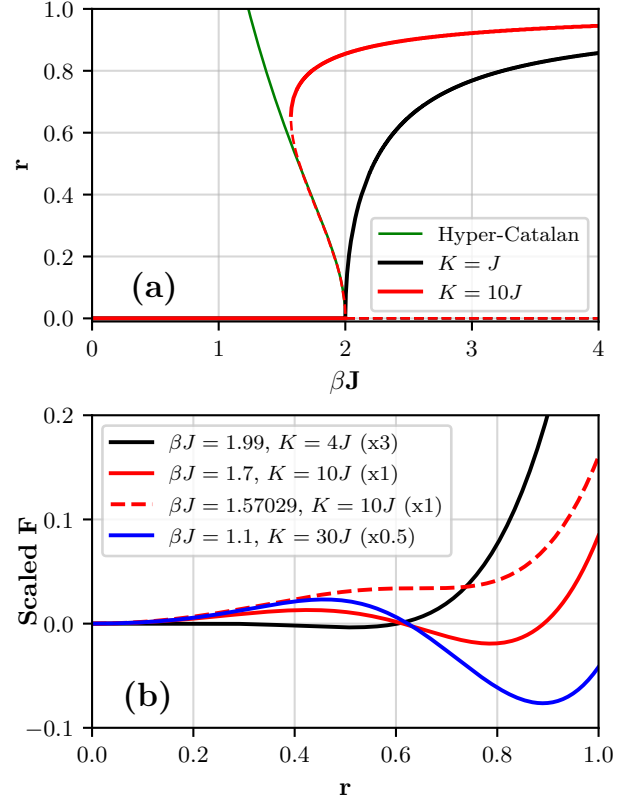


FIG. 1. (a) Order-parameter bifurcation for mixed  $J$ - $K$  coupling. Solid curves plot the stationary solutions of  $r = g(X(x, r; C))$  versus  $x = \beta J$  for two coupling ratios:  $C = K/J = 1$  (black) and  $C = 10$  (red). Stable (solid lines) and unstable (dashed lines) are shown. The green line overlaying the red saddle is the hyper-Catalan series Eq. (29) truncated at  $O(r^6)$ , demonstrating analytic agreement with the numerical unstable branch. At  $x = 2$  the model with  $K = J$  undergoes a super-critical pitchfork bifurcation, whereas the quartic-dominated case ( $K = 10J$ ) exhibits a sub-critical bifurcation with a finite coexistence interval and hysteresis. (b) Free-energy profiles plotted against the order parameter  $r$  for four illustrative pairs  $(C, \beta J)$ :  $\{4, 1.99\}$ ,  $\{10, 1.70\}$ ,  $\{10, 1.57029\}$ , and  $\{30, 1.10\}$ . Each curve is multiplied by the indicated factor (in parentheses) so that the minima can be identified. For  $C = 4, \beta J = 1.99$  the system is near tricriticality, with minima at  $r \approx 0$  and  $r \approx 0.53$  separated by a vanishing barrier; for  $C = 10, \beta J = 1.70$  a clear first-order double-well appears (barrier at  $r \approx 0.43$ , stable well at  $r \approx 0.79$ ); at the saddle-node point  $C = 10, \beta J = 1.57029$  the nonzero extrema coalesce at  $r \approx 0.64$ ; and for  $C = 30, \beta J = 1.10$  the barrier ( $r_u \approx 0.46$ ) and deep well ( $r_s \approx 0.89$ ) illustrate a strongly first-order landscape.

potential downwards and destabilize the newly born minimum. Stability is restored by the positive sixth-order coefficient  $a_6$ , so the leading nonlinear competition is now

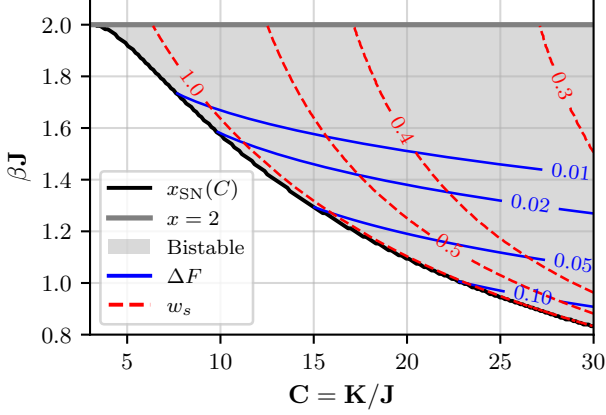


FIG. 2. Energetic and dynamical landscape of the mixed  $J$ - $K$  Kuramoto memory in the  $(C, x)$ -plane, where  $C \equiv K/J > 3$  and  $x \equiv \beta J$ . Solid blue lines are iso-barrier contours of  $\Delta F(C, x) = F(x, C, r_u) - F(x, C, 0)$ , the activation energy separating the incoherent metastable state ( $r = 0$ ) from the stable memory minimum ( $r = r_s$ ); numerical labels indicate the corresponding  $\Delta F$  values. Dashed red lines show the basin-width proxy  $w_s(C, x) = \sqrt{1/F''(x, C, r_s)}$ , the inverse curvature at the stable well at  $r = r_s$ . The shaded band marks the bistable window  $x_{\text{SN}}(C) < x < 2$ : its lower boundary (grey line) is the saddle-node locus  $x_{\text{SN}}(C)$  where the non-trivial pair  $(r_s, r_u)$  is born, while its upper boundary at  $x_P = 2$  is the spinodal where  $r = 0$  loses linear stability.

between the negative  $r^4$  and the positive  $r^6$  terms. In this regime the free energy develops two extra minima separated by a barrier, and the system undergoes a first-order transition, with a finite jump of  $r$ , at a temperature below  $T_c$ . Thus the small- $r$  Landau expansion of the mean-field free energy explains why the incoherent-to-coherent transition is continuous when  $K < 3J$  and turns first order once the four-body coupling exceeds the pairwise coupling; the equality  $K = 3J$  locates the tricritical point where the nature of the transition changes.

In a multidimensional parameter space, here the plane spanned by temperature  $T$  (or frequency spread  $\Delta$ ; see below) and the coupling ratio  $C = K/J$ , a tricritical point is the unique thermodynamic state at which a line of continuous (second-order) phase transitions meets a line of discontinuous (first-order) transitions. In the higher-order Kuramoto associative memory this special point separates the soft-switch regime ( $K < 3J$ , continuous onset, large accessibility) from the latch-like regime ( $K > 3J$ , explosive synchronization with hysteresis, high robustness).

In summary, we have three regimes for associative memory. (1) Continuous (soft) recall for  $K < 3J$ : easy retrieval from small cues, smooth onset. (2) Tricritical regime at  $K \approx 3J$ . (3) Explosive (hard) recall for  $K > 3J$ : robust memory attractors and high capacity, at the cost of requiring finite cues. One should maintain

$J > 0$  to ensure linear destabilization of the incoherent state, and tune  $K$  relative to  $J$  to sculpt the basins of attraction and maximize capacity without losing accessibility.

### Dynamical Mean-Field approximation

Alternatively, we can obtain a dynamical mean-field approximation in the continuum limit with Lorentzian frequency distribution of mean  $\omega_0$  and half-width  $\Delta$

$$g(\omega) = \frac{\Delta}{\pi[(\omega - \omega_0)^2 + \Delta^2]}, \quad (14)$$

following the Ott-Antonsen ansatz [33]. Under the Lorentzian frequency distribution the Ott-Antonsen ansatz confines the dynamics to the invariant manifold where the evolution of the entire population is governed by  $z(t)$ ; in particular, one obtains  $\dot{\psi}(t) = \omega_0$ . So the centroid phase  $\psi$  advances at the mean natural frequency while the modulus  $r(t)$  encodes the synchrony generated by the mixed  $J$ - $K$  interactions [7, 33]

$$\dot{r} = -\Delta r + \frac{J}{2} r (1 - r^2) + \frac{K}{12} r^3 (1 - r^2). \quad (15)$$

Setting  $\dot{r} = 0$  gives a polynomial in  $r^2$  whose stable and unstable branches can be written in closed form

$$r = \pm \sqrt{\frac{K - 6J \pm \sqrt{(6J + K)^2 - 48\Delta K}}{2K}}. \quad (16)$$

This equation should be reconciled with the equilibrium functional  $F(r)$ . Indeed, the order-parameter dynamics of a Kuramoto ensemble can be written as a gradient flow  $\tau \dot{r} = -\partial F / \partial r$  of the free energy  $F(r) = \beta f(r)$ , where  $\tau$  is a time scale. For the mean-field Hamiltonian  $H$  the equilibrium functional  $F(r)$  is given by Eq. (10) and  $-\partial F / \partial r$  expanded in small  $r$  is by Eq. (12) multiplied by  $\beta$ . Up to cubic order the only linear term that survives is  $-\beta J(1 - \beta J/2)r$ , which vanishes at the critical line  $\beta J = 2$  as it should.

For a Lorentzian frequency distribution of half-width  $\Delta$  the OA reduction gives Eq. (15) and comparing it with Eq. (12) shows that an exact identification  $\tau \dot{r} = -\partial F / \partial r$  is possible near the bifurcation ( $r \ll 1$ ) if we set

$$\Delta = 1/\beta = T \quad \text{and} \quad \tau = \beta^2 J. \quad (17)$$

Equilibrium  $XY$  theory, on the other hand, is controlled by the temperature  $T = 1/\beta$ , i.e. the strength of additive angular noise in a Langevin formulation. Identifying  $\Delta = T$  means equating the characteristic scale of quenched frequency spread with that of annealed thermal agitation; both enter the linear stability of  $r$  in formally the same way, namely as a negative drift proportional



to  $r$ . This replacement is therefore reasonable near the onset of synchronization, where only the first-order coefficient matters. Beyond the linear neighborhood, however, the two notions of disorder are physically distinct: thermal noise preserves detailed balance, while frequency heterogeneity does not.

Such higher-order coupling terms have also been explored in networks of spiking or bursting neurons, where adding triadic interactions was shown to reduce the effective synchronization cost and enable robust multistable behavior [34].

### Analytic construction of the saddle-node line

Next, we analytically construct the saddle-node line in  $C \equiv K/J > 3$  regime. Define  $X(x, r; C) = xr + \frac{Cxr^3}{6}$ , where  $x \equiv \beta J$ . Fixed points satisfy

$$r = \frac{I_1(X)}{I_0(X)} \equiv g(X), \quad (18)$$

and a saddle-node (fold) occurs when

$$\frac{d}{dr} g(X(x, r; C)) = 1. \quad (19)$$

Solving Eqs. (18)–(19) yields the critical pair  $(x_{SN}(C), r_{SN}(C))$ . Fig. 1(a) plots the stable (solid) and unstable (dashed) solutions of Eq. (18); where the solid and dotted lines meet marks the fold.

*Cusp at  $C=3$ .* Expanding the Bessel ratio  $I_1(X)/I_0(X) = \frac{1}{2}X - \frac{1}{16}X^3 + \frac{1}{96}X^5 + \dots$  and using Eq. (18) yields, after truncation at  $O(r^6)$  and dividing by  $r(1 - x/2)$  the polynomial

$$0 \approx 1 - l_0 r^2 + m_0 \left( \frac{x^2}{48} - \frac{C}{16} \right) r^4 + m_0 \left( \frac{5Cx^2}{288} - \frac{11x^4}{3072} - \frac{C^2}{96} \right) r^6 \quad (20)$$

where  $l_0 = \frac{x}{x-2} \left( \frac{x^2}{8} - \frac{C}{6} \right)$  and  $m_0 = x^3/(x-2)$ . Writing  $C = 3 + \delta$  ( $\delta > 0$ ) and  $x = 2 - \varepsilon$  with  $\varepsilon = O(\delta^2)$ , one finds that the first non-trivial balance occurs at  $r^2 = \delta/5 + O(\delta^2)$ , hence

$$r_{SN}(C) = \sqrt{\frac{\delta}{5}} + O(\delta), \quad x_{SN}(C) = 2 - \frac{\delta^2}{30} + O(\delta^3). \quad (21)$$

The absence of a linear term in  $x_{SN} - 2$  confirms that  $(C, x, r) = (3, 2, 0)$  is a cusp (codimension-2) point; the fold line emerges tangentially with a quadratic shift, while the new branch  $r_{SN} > 0$  grows with the square-root characteristic of a saddle-node.

*Asymptotes for  $C \rightarrow \infty$ .* When  $C \gg 1$  the cubic term in  $X$  is dominant, so any finite fixed-point solution must satisfy  $xr = O(C^{-1})$ . Set

$$x = \frac{\kappa}{C}, \quad r \rightarrow r_\infty \in (0, 1), \quad X \rightarrow X_\infty = \frac{\kappa}{6} r_\infty^3, \quad (22)$$

where  $\kappa = O(1)$  to be determined. Insert Eq. (22) into the fixed-point condition Eq. (18) and into the tangency condition Eq. (19); the latter reads  $g'(X_\infty) \left( x + \frac{Cx r_\infty^2}{2} \right) = 1$ . Because  $x = \kappa/C$  the  $x$  term is negligible and one obtains  $g'(X_\infty) \frac{C}{2} x r_\infty^2 = 1$ , i.e.  $g'(X_\infty) \kappa r_\infty^2 / 2 = 1$ . Using the Bessel identity  $g'(X) = \frac{1}{2}(1 - g(X)^2)$  and the fixed-point relation  $g(X_\infty) = r_\infty$  gives

$$\frac{1}{2}(1 - r_\infty^2) \frac{\kappa r_\infty^2}{2} = 1 \implies \kappa = \frac{6}{r_\infty^2(1 - r_\infty^2)}. \quad (23)$$

Equations (22) and (23) form the closed system

$$r_\infty = g(X_\infty), \quad X_\infty = \frac{\kappa}{6} r_\infty^3, \quad \kappa = \frac{6}{r_\infty^2(1 - r_\infty^2)}, \quad (24)$$

which involves a single unknown  $r_\infty \in (0, 1)$ . Solving numerically yields

$$r_{SN}(C) \xrightarrow{C \rightarrow \infty} r_\infty \simeq 0.77733, \quad x_{SN}(C) \sim \frac{33.454}{C}. \quad (25)$$

Therefore, as  $C$  grows the bifurcation in  $x$  retreats toward zero, reflecting the fact that an ever-weaker pairwise drive suffices once the quartic term dominates. Conversely, the critical overlap approaches a constant: even in the strong-quartic limit the ordered branch is born with  $r \simeq 0.78$ , so a finite cue amplitude is still required to cross the saddle: large  $C$  does not eliminate the activation threshold, it merely shifts the bifurcation leftward (cf. Fig. 1(b)).

*Hyper-Catalan series for unstable branch* To analytically study the unstable branch for the intermediate values of  $C$ , we can use the hyper-Catalan series expansion [35] as solutions to Eq. (20). The notation  $\alpha = l_0 r^2$  brings Eq. (20) into the standard form of the cubic equation in  $\alpha$  used in [35]

$$0 = 1 - \alpha + t_2 \alpha^2 + t_3 \alpha^3, \quad (26)$$

with

$$t_2 = \frac{12x(x-2)(x^2-3C)}{(4C-3x^2)^2}, \quad (27)$$

$$t_3 = \frac{3(x-2)^2(96C^2-160Cx^2+33x^4)}{2(4C-3x^2)^3}. \quad (28)$$

The unstable (small- $r$ ) solution of (18) admits the hyper-Catalan expansion to the sixth order in  $r$  (unstable root)

$$r_u^2 = l_0^{-1} (1 + t_2 + 2t_2^2 + 5t_2^3 + t_3 + 5t_2 t_3 + 21t_2^2 t_3 + 3t_3^2 + 28t_2 t_3^2 + 12t_3^3). \quad (29)$$

In Fig.1(a), the green curve shows Eq.(29) truncated at sixth order in  $r$ , which accurately matches the numerical solution throughout the bistable region  $x_{\text{SN}}(C) < x < 2$ , enabling analytical calculation of the barrier height and the coexistence of two stable states.

### Kramer Escape Time in Higher-Order Kuramoto Networks

In the mixed  $J$ - $K$  Kuramoto model the macroscopic order parameter  $r$  evolves on the one-dimensional free-energy landscape  $F(r) = \beta f(r)$  with  $f(r)$  given by Eq. (12). It serves as the coarse-grained free-energy density of the mean-field ensemble, so the depth of any metastable well is measured relative to the neighboring saddle on the same one-dimensional landscape. Two relevant minima coexist inside the bistable strip  $x_{\text{SN}}(C) < x < 2$ : the incoherent state at  $r = 0$  and the memory state at  $r = r_s(C, x)$ . They are separated by the saddle  $r = r_u(C, x)$ . Additive noise (thermal fluctuations) can drive the system from either minimum over the intervening saddle at  $r = r_u(C, x)$ .

Evaluating  $F(r)$  at the unstable root  $r_u$  therefore gives the height of the escape barrier from either the incoherent minimum at  $r = 0$  or from the memory state at  $r = r_s$ . Therefore, we define two quantities  $\Delta F = F(r_u) - F(0) = F(r_u)$  and  $\Delta \mathcal{F} = F(r_u) - F(r_s)$ . We should also pay attention to the special  $x = x_{\text{coex}}(C)$  where  $F(r_s) = F(0)$ : here the two minima, namely incoherent ( $r = 0$ ) and memory ( $r = r_s$ ) have equal depth ("coexist"), so  $\Delta F = \Delta \mathcal{F}$  equals the height of the saddle itself. We define the curvature widths of the stable and saddle points

$$w_0 = \frac{1}{\sqrt{F''(0)}}, w_s = \frac{1}{\sqrt{F''(r_s)}}, w_u = \frac{1}{\sqrt{|F''(r_u)|}}, \quad (30)$$

for the incoherent state  $r = 0$ , the stable  $r = r_s$  and the saddle points  $r = r_u$ , respectively.

The escape from the either of the stable states across the barrier is controlled by the Kramer escape time [36, 37] so that the first passage time out of the stable  $r = r_s$  basin is

$$\tau_{\text{esc}} \simeq 2\pi w_s w_u \exp[\beta N \Delta \mathcal{F}(C, x)] \tau_0, \quad (31)$$

where  $\tau_0 = 2\pi/\omega_0$  is the natural oscillation period. For the escape from the incoherent  $r = 0$  state we need to replace  $w_s \rightarrow w_0$  and  $\Delta \mathcal{F} \rightarrow \Delta F$ .

*Near the tricritical line.* Write  $C = 3 + \delta$  and  $x = 2 - \varepsilon$  with  $\varepsilon = O(\delta^2)$  inside the bistable strip. Using the leading expansion  $r_u^2 = (3\varepsilon)/\delta + O(\varepsilon^2)$  obtained from Eq. (29), one finds

$$\Delta F = \frac{3}{4} \frac{\varepsilon^2}{\delta} + O(\varepsilon^3, \delta \varepsilon^2). \quad (32)$$

At coexistence the wells satisfy  $\varepsilon_{\text{coex}} = \delta^2/30$ , so  $\Delta F_{\text{coex}} = (3/4)\delta^3/30^2$ , recovering the cubic scaling  $\Delta F \propto (C - 3)^3$  observed numerically.

*Large- $C$  limit.* For  $C \gg 1$  with  $x = \kappa/C$  the hyper-Catalan variables obey  $t_2 = O(C^{-2})$  and  $t_3 = O(C^{-1})$  and Eq. (29) reduces to  $r_u^2 \simeq 1/l_0$  with  $l_0 \simeq \kappa/12$ . Hence

$$r_u \simeq \sqrt{\frac{12}{\kappa}}, \quad C \gg 1. \quad (33)$$

As  $C \gg 1$  ( $\kappa \rightarrow 33.454$ ) one obtains  $r_u \rightarrow 0.6$ , in quantitative agreement with Fig. 2. The barrier height approaches the constant plateau

$$\Delta F_{C \gg 1} \simeq \frac{\kappa}{8} r_u^4 - \log \left( I_0 \left( \frac{\kappa}{6} r_u^3 \right) \right) \rightarrow 0.2. \quad (34)$$

that limits the right-hand side of Fig. 2.

Figure 2 illustrates the  $J - K$  Kuramoto model in the  $(C, x)$  plane. Solid blue contours encode the activation barrier  $\Delta F(C, x)$  that controls the Kramer escape time [36, 37], while dashed contours plot the basin-width proxy  $w_s(C, x) = 1/\sqrt{F''(r_s)}$ , a measure of retrieval speed and tolerance to noise. The grey curve marks the saddle-node locus  $x_{\text{SN}}(C)$ ; together with the upper spinodal  $x = 2$  it delimits the bistable strip in which memory and incoherent states coexist. Vertical slices through Fig. 2 (increasing  $x$  at fixed  $C$ ) reveal that both the barrier height  $\Delta F$  and the basin width  $w_s$  shrink with temperature. As a result, retrieval becomes faster, but at the cost of reduced robustness, as memories escape more quickly under noise. A horizontal scan (increasing  $C$  at fixed  $x$ ) shows the same qualitative trend: increasing the quartic-to-pairwise ratio accelerates convergence, but shortens retention and requires the cue to start closer to the memory.

At the balanced operating point  $(C, x) = (10, 1.7)$ , for example, the stable and unstable states occur at  $r_s \approx 0.79$  and  $r_u \approx 0.43$ , yielding  $\Delta \mathcal{F} \approx 0.032$  and  $w_s \approx 0.63$ . With  $N = 500$  oscillators and  $\beta = 1$ , the extensive barrier  $N \Delta \mathcal{F} \approx 16$  leads to a Kramers escape time of roughly  $\tau_{\text{esc}} \sim 5e^{16} \tau_0 \approx 4.5 \times 10^7 \tau_0$ , ensuring long memory lifetimes.

On the Ott-Antonsen (OA) manifold, the macroscopic amplitude obeys Eq. (15). Linearizing around the stable state  $r = r_s$  yields exponential convergence  $\dot{\delta}r = -\lambda \delta r$ , where  $\lambda = F''(r_s) = 1/w_s^2$ . For instance, with  $w_s = 0.63$ , we find  $\lambda \approx 2.5$ , so ten e-folds of convergence occur in

$$\tau_{\text{recall}} \simeq \frac{10}{\lambda} \tau_0 \approx 4 \tau_0, \quad (35)$$

confirming ultra-fast deterministic retrieval. The operating point at  $(10, 1.7)$  therefore combines  $\tau_{\text{recall}} \lesssim 10 \tau_0$  with  $\tau_{\text{esc}} \sim 10^7$ – $10^8$  intrinsic cycles, providing both rapid pattern completion and long error-free retention: comfortably longer than the coherence time of modern photonic or superconducting oscillator hardware [11].

The trends in Fig. 2 are governed by Eq. (31), with the intensive barrier  $\Delta F$  replacing the extensive  $\Delta \mathcal{F}$ . Increasing either  $x$  or  $C$  reduces both the barrier height  $\Delta F$  and the local curvature  $F''(r_u)$ , thereby shortening  $\tau_{\text{esc}}$  while leaving the convergence rate  $\lambda$  nearly unaffected. In contrast, approaching the tricritical cusp ( $C \downarrow 3$ ) causes the barrier to diverge as  $\Delta F \propto (C - 3)^3$ , dramatically extending retention time.

Most importantly, all quantities as barriers  $\Delta F$ ,  $\Delta \mathcal{F}$ , curvatures  $w_s$ ,  $w_u$ , and OA rates are available. This tractability enables educated tuning of  $(J, K, \beta)$  to engineer desired trade-offs between recall speed, robustness, and memory lifetime.

### Mean-Field Theory with Pattern Interference

To quantify retrieval under finite load we incorporate the interference of the  $P - 1$  non-condensed patterns into a noisy mean-field description. Writing Eq. (6) in terms of the complex overlaps  $r_\mu e^{i\phi_\mu} = N^{-1} \sum_j \xi_j^\mu e^{i\theta_j}$  yields

$$\dot{\theta}_i = \omega_i + \frac{1}{P} \sum_{\mu=1}^P \left( J r_\mu + \frac{K}{6} r_\mu^3 \right) \xi_i^\mu \sin(\phi_\mu - \theta_i). \quad (36)$$

Without loss of generality we assume that pattern  $\mu = 1$  is being retrieved ( $\xi_i^1 \equiv 1$  after a binary gauge rotation). For the remaining patterns the overlaps satisfy  $r_\mu = \mathcal{O}(N^{-1/2})$  when no external cue is given. Under this scaling the central-limit theorem applies and the summed contribution of the  $P - 1$  terms can be modeled as a Gaussian random field. Splitting the signal and noise parts yields

$$\dot{\theta}_i = \omega_i + \frac{1}{P} \left( J r + \frac{K}{6} r^3 \right) \sin(\phi - \theta_i) + \eta_i, \quad (37)$$

where  $r \equiv r_1$ ,  $\phi \equiv \phi_1$  and the crosstalk field  $\eta_i = \frac{1}{P} \sum_{\mu=2}^P (J r_\mu + \frac{K}{6} r_\mu^3) \xi_i^{(\mu)}$  is Gaussian with zero mean. Its variance is obtained by averaging over the random bits and over the distribution of the small overlaps:

$$\begin{aligned} \sigma^2 &= \frac{\alpha N}{P} \mathbb{E} \left[ \left( J r_\mu + \frac{K}{6} r_\mu^3 \right)^2 \right] \\ &= \frac{\alpha}{P} \left( J^2 + \frac{2JK}{3N} + \frac{5K^2}{12N^2} \right), \end{aligned} \quad (38)$$

where  $\alpha = P/N$  and we used the large- $N$  moments  $\mathbb{E}[r_\mu^2] = 1/N$ ,  $\mathbb{E}[r_\mu^4] = 2/N^2$ ,  $\mathbb{E}[r_\mu^6] = 15/N^3$ . In the thermodynamic limit  $\sigma^2 \rightarrow \alpha J^2/P$ , while the  $K$ -dependent corrections become important only for finite  $N$  or for  $K \gg J$ .

The effective local field experienced by each oscillator therefore has deterministic component  $h = J r + \frac{K}{6} r^3$  and Gaussian noise  $\eta \sim \mathcal{N}(0, \sigma^2)$ . Notably, the variance  $\sigma^2$  and the coupling tensors  $J_{ij}$ ,  $K_{ijkl}$  scale with  $1/P$ , which would normally suppress the interactions as the number

of stored patterns increases. However, rather than interpreting this suppression as a weakening of the couplings, we absorb the  $1/P$  scaling into the effective temperature, treating it as an increase in thermal fluctuations with load. This perspective allows us to fix the effective temperature  $\beta$  and drop the explicit  $1/P$  factor in the couplings.

Following the standard Legendre construction, the resulting intensive free energy at fixed effective noise reads

$$f(r) = \frac{J}{2} r^2 + \frac{K}{8} r^4 - \frac{1}{\beta} \int Dz \ln I_0[\beta(h + \sigma z)], \quad (39)$$

with  $Dz = (2\pi)^{-1/2} e^{-z^2/2} dz$ . The self-consistency equations are

$$r = \int Dz \frac{I_1[\beta(h + \sigma z)]}{I_0[\beta(h + \sigma z)]}, \quad \frac{\partial f}{\partial r} = 0, \quad (40)$$

which generalize Eq. (10) to finite load. As  $\alpha$  (and hence  $\sigma$ ) increases, the retrieval minimum at  $r > 0$  becomes shallower as observed in Fig. 3. Therefore the pattern load  $\alpha$  increases the critical point for the pitchfork bifurcation  $x_P > 2$ . To look at it from a different perspective, the retrieval minimum vanishes at a critical load  $\alpha_c(J, K)$  defined by  $f''(r = 0) = 0$ . Expanding Eq. (39)

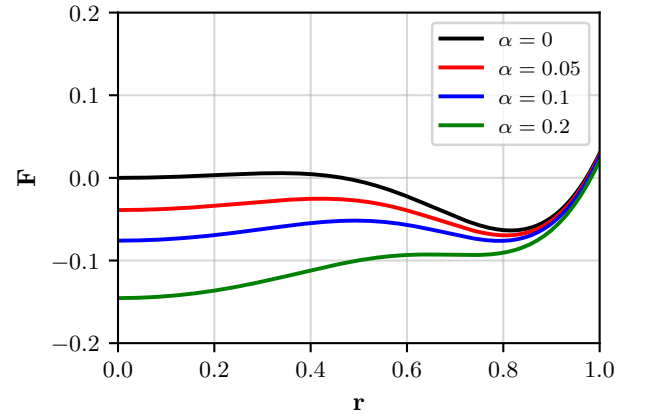


FIG. 3. Mean-field free energy landscape  $f(r)$  Eq. (39) as a function of the overlap  $r$ , plotted for increasing values of the pattern load  $\alpha$  at fixed  $\beta J = 1.79$ , and  $K = 10J$ . As  $\alpha$  increases, crosstalk noise flattens the free energy and lowers the depth of the retrieval minimum. Beyond a critical load, the nonzero minimum disappears and the system undergoes a transition to a disordered phase where memory retrieval fails.

to quadratic order gives  $f''(0) = \frac{1}{2}\beta(J - \beta^{-1}) + \frac{1}{4}\beta K \alpha$ , which yields the analytic estimate

$$\alpha_c = \frac{2}{K} (\beta J - 1) \quad (\text{for } \beta J > 1). \quad (41)$$

This formula agrees with the disappearance of the non-zero minimum in Fig. 3 and shows explicitly how



the quartic coupling enhances capacity: at fixed  $J$  the critical load scales as  $\alpha_c \propto 1/K$ .

In the zero-temperature limit ( $\beta \rightarrow \infty$ ),  $\ln I_0(\beta x) \simeq \beta|x|$ , and averaging over  $z$  gives the free-energy density

$$F_{T=0}(r) = \frac{J}{2}r^2 + \frac{K}{8}r^4 - J \left[ \sqrt{\frac{2\alpha}{\pi}} e^{-h^2/(2\sigma^2)} + h \operatorname{erf}(h/\sqrt{2\sigma^2}) \right], \quad (42)$$

with  $h = Jr + \frac{K}{6}r^3$  and  $\sigma^2$  from Eq. (38). Even at  $J = 0$  the term proportional to  $K^2\alpha/N^2$  ensures a non-zero variance, so quartic-only memories remain susceptible to pattern interference, albeit at a reduced level.

### LARGE-SCALE NUMERICAL SIMULATIONS FOR MEMORY RETRIEVAL

In this section, we present large-scale simulations to test the mean-field predictions developed in the previous sections. Our goals are to validate the predicted bifurcation structure for small pattern load, explore retrieval dynamics in the presence of finite crosstalk noise, and empirically measure the memory capacity.

#### Efficient Simulation of Higher-Order Dynamics

To simulate Eq. (6) efficiently, we avoid explicitly forming the full four-body Hebbian tensor  $K_{ijkl}$ , which would require  $\mathcal{O}(N^4)$  memory and computation. Instead, we exploit the binary nature of the stored patterns  $\xi_i^\mu \in \{\pm 1\}$  and rewrite the interaction terms using global pattern overlaps.

Specifically, we define the complex overlaps

$$S_+^\mu = \sum_j \xi_j^\mu e^{i\theta_j}, \quad S_-^\mu = \overline{S_+^\mu}, \quad (43)$$

and express the quartic interaction term as:

$$\frac{K}{PN^3} \sum_{\mu=1}^P \xi_i^\mu \operatorname{Im} [(S_+^\mu)^2 S_-^\mu e^{-i\theta_i}]. \quad (44)$$

This reduces the computational cost to  $\mathcal{O}(PN)$  per timestep, both in memory and runtime.

For fixed  $J$  and  $K$ , temperature can be incorporated in two dynamically equivalent ways at equilibrium: (i) by Langevin dynamics, where we add thermal noise  $\eta_i(t)$  with  $\langle \eta_i(t)\eta_j(t') \rangle = 2D\delta_{ij}\delta(t-t')$  and set  $D = 1/\beta$ , (ii) by drawing the natural frequencies  $\omega_i$  from a Lorentzian distribution:  $g(\omega)\Delta/\pi[(\omega - \omega_0)^2 + \Delta^2]$ , where  $\Delta = 1/\beta$  controls the width of the distribution, and hence the level of disorder.

### Validation of Mean-Field Theory Under Varying Memory Load

To validate the equilibrium mean-field approximation, we compare theoretical predictions to numerical simulations in the low-load regime. Using large networks ( $N = 500$ ) with a single stored pattern ( $P = 1$ ) minimizes fluctuations and ensures stable attractor dynamics. In this setting the mean-field theory is well justified and expected to accurately describe the system's behavior.

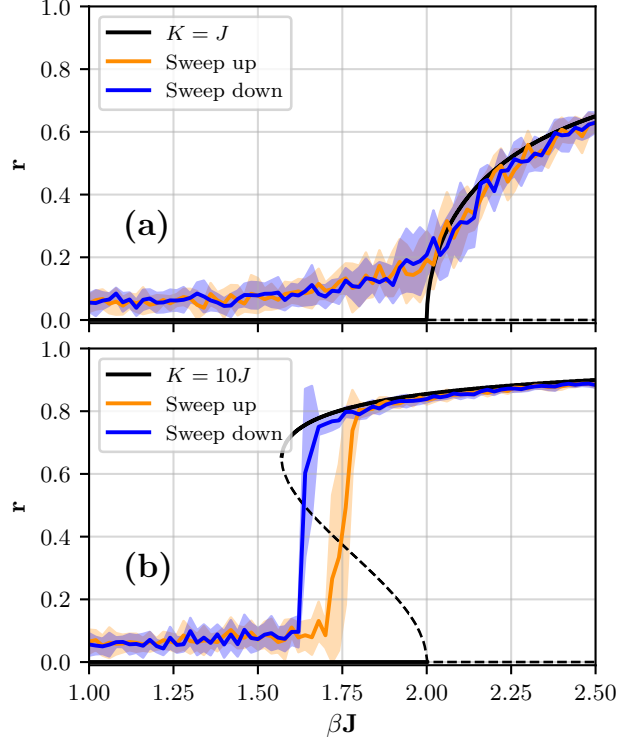


FIG. 4. Upward (blue) and downward (orange) sweeps of  $\beta J$  for a network with  $N = 500$  storing a single pattern ( $P = 1$ ), at fixed coupling ratios  $K/J = 1$  (top) and  $K/J = 10$  (bottom), using a sweep rate of  $d(\beta J)/dt = 10^{-4}$ . The system is initialized in a random initial state before being allowed to evolve by Eq. (6) with Langevin noise. Each curve shows the average of 20 trials, with shaded regions denoting their variance. Black curves show mean-field predictions from Eq. (11). For small  $K/J$ , the system undergoes a continuous supercritical pitchfork bifurcation consistent with mean-field theory. At larger  $K/J$ , the system exhibits a discontinuous jump and hysteresis, indicating bistability due to stronger higher-order interactions.

Figure 4 shows the qualitative shift in dynamics as  $K/J$  increases. At low ratios of  $K/J < 3$ , the transition of the order parameter is continuous, resembling a pitchfork bifurcation. As  $K/J$  increases, the transition becomes discontinuous and a noticeable hysteresis loop emerges. This behavior indicates the emergence of metastable states and a first-order phase transition.

The numerical results closely follow the mean-field predictions, confirming the theoretical analysis in the low pattern load regime.

We then turn to the case of finite pattern load  $\alpha = P/N$ . At fixed network size  $N$  increasing  $P$  introduces quenched noise by other patterns and competing overlaps. In Fig. 5 theoretical results and numerical findings for a pattern load  $\alpha = 0.15$ , a regime where the assumptions for the noise mean field theory should still hold, are shown.

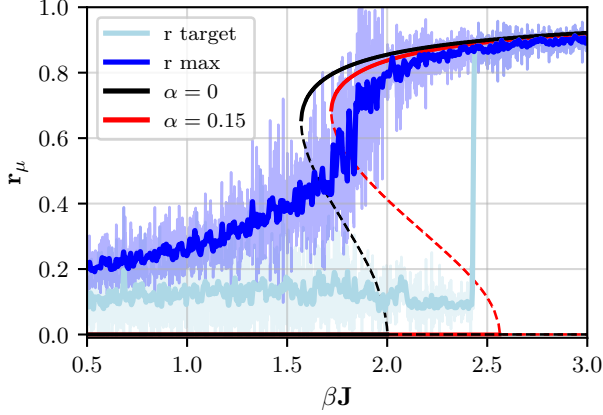


FIG. 5. Downward sweep of  $\beta J$  for memory load  $\alpha = 0.15$  with coupling ratio  $K/J = 10$  at sweep rate  $d(\beta J)/dt = 10^{-5}$ . Simulations were performed with  $N = 100$  oscillators storing  $P = 15$  random patterns. The system is initialized in a pattern state before being allowed to evolve by Eq. (6) with Langevin noise. We plot the overlap with the pattern in light blue and the maximum overlap with any patterns in dark blue. Results are shown from a single run, smoothed with a Gaussian filter; shaded regions indicate raw deviations. Mean-field predictions with noise (red, Eq. (40)) and without noise (black, Eq. (11)) are shown for comparison. A transition, marked by loss of overlap with the target pattern and rising overlap with a competing pattern, occurs well before the noiseless bifurcation point, indicating destabilization from crosstalk noise.

In black we plot the bifurcation diagram predicted by the static mean field analysis without crosstalk in black and with crosstalk in red. We see that incorporating the pattern load  $\alpha$  increases the critical point for the pitchfork bifurcation  $x_P$ . Interestingly the upper stable branch is mostly effected close to the saddle node bifurcation, but the results are very similar in the regime where only the non zero solution is stable. Numerically, we observe that the target pattern (light blue) is initially retrieved, but as  $\beta J$  decreases, the system spontaneously switches to another attractor (blue), corresponding to a different stored pattern. This transition occurs well before the noiseless mean-field theory predicts instability, underscoring the impact of crosstalk noise on retrieval dynamics. The leading-order parameter closely follows the predictions of the noisy mean-field theory, consistent

with a model in which all stored patterns are equivalent.

### Capacity Scaling

An essential measure of memory performance is the capacity scaling, which quantifies how the number of patterns that can be reliably stored and retrieved scales with the size of the network. To empirically estimate this, we fix a network size  $N$ , then vary the number of stored patterns  $P$ , and evaluate retrieval performance. For each  $N$  we generate  $P$  random patterns, select one, and create a corrupted input with an overlap  $\epsilon$  by randomly phase-shifting  $\epsilon/2$  of the oscillators by  $\pi$ . The network is then allowed to evolve from this input under its dynamics for a time  $T$ , long enough to ensure convergence. We then calculate the final overlap with the original distorted pattern and average this final overlap over  $N_{\text{trial}}$  independent trials to compute the retrieval rate  $\chi$  as a function of  $P$ . The largest  $P$  value for which retrieval rate remains consistently over a certain threshold  $\chi \geq \chi_c$ , defines the empirical capacity at that  $N$ . Repeating this process across multiple network sizes reveals how capacity scales with  $N$ .

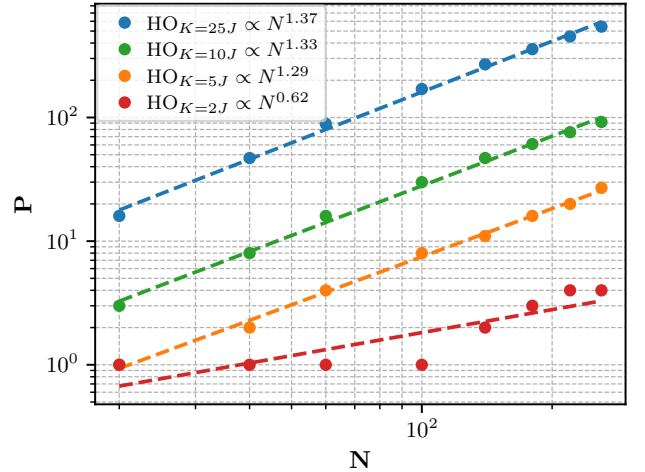


FIG. 6. Capacity scaling of the higher-order (HO) Kuramoto model at finite temperature. The system is setup in a random initial condition with 0.95% overlap to a target pattern and allowed to evolve after the dynamics of Eq. (6) for a long enough time for the system to converge. By calculating the absolute value of the overlap to the original pattern at the end and averaging over  $N_{\text{trials}} = 100$  we measure the highest number of patterns stored in a network of size  $N$  such that retrieval rate  $\chi \geq 0.85$ . The coupling  $J$  is fixed such that  $\beta J = 4$ , and we vary  $K/J = 2$  (red), 10 (orange), 20 (green) and 25 (blue). Superlinear scaling emerges clearly for  $K/J \gg 1$ .

In Fig. 6 we depict the storage capacity of the higher-order Kuramoto network at finite temperature. Superlinear scaling survives thermal noise provided the quartic coupling dominates, i.e. when the ratio  $C \equiv K/J$

exceeds the tricritical threshold  $C_{\text{tri}} = 3$ . Retrieval becomes possible as soon as  $x = \beta J$  crosses the lower saddle-node  $x_{\text{SN}}(C)$ , where a pair of non-trivial fixed points  $(r_u, r_s)$  is created. Optimal capacity is achieved for  $x > x_P(C)$ , the pitchfork (linear-stability) threshold at which the incoherent maximum  $r = 0$  disappears and the system relaxes monotonically into the single minimum  $r = r_s$ ; the quartic term then deepens this well and enhances noise robustness. Operating inside the bistable window  $x_{\text{SN}} < x < x_P$  slows convergence and may trap weak cues in the incoherent state.

Figures 4 and 5 show that increasing the pattern load  $\alpha$  mainly shifts the pitchfork point  $x_P$  to higher values, while the upper stable branch  $r_s$  is scarcely affected; consequently, for strongly quartic couplings ( $C \gtrsim 10$ ) the superlinear regime becomes increasingly insensitive to  $\alpha$ . Although retrieval is possible with  $J = 0$ , it then requires much larger  $K$ ; introducing a moderate pairwise term therefore widens the practical domain of retrieval, while further enlarging  $C$  still yields incremental gains in capacity.

In Fig. 7, we present numerical results for the zero-temperature limit ( $T = 0$ ). We observe that when the ratio  $K/J$  is sufficiently large, the higher-order Kuramoto model outperforms the second-resonance Kuramoto model (4) in terms of capacity scaling. The best performance is achieved in the extreme case  $J = 0$ , where the dynamics are entirely governed by the higher-order interaction. In this regime, the system exhibits clear polynomial scaling, and this suggests that higher-order interactions alone can give rise to attractor dynamics with high storage capacity in the absence of noise.

Although the single-well regime  $\beta J > x_P$  at high  $C$  is optimal for digital, non-volatile storage with nanosecond-scale recall, the single well regime at moderate  $C$  and the bistable region  $x_{\text{SN}}(C) < \beta J < x_P$  are not without merit; they become preferable whenever the task demands analog similarity processing, energy-efficient switching, or rich transient dynamics. In this range the ordered branch emerges continuously (for  $C < 3$ ) or via a soft saddle-node (for  $C > 3$  in the bistable region), so the order parameter  $r(t)$  follows the overlap of the cue instead of saturating abruptly. Partial or noisy inputs therefore converge to intermediate values of  $r$ , making the network useful for graded completion, fuzzy nearest neighbor retrieval and associative hashing, where maintaining balance between cue strength and network response is more important than strict winner-take-all behavior. When the free-energy wells are shallow and the barriers are low, the microscopic torques required to move between attractors are correspondingly low; this translates into reduced power dissipation and faster reconfiguration, a property desirable in adaptive control loops or online learning systems that must update their internal state frequently. Finally, just below the pitchfork bifurcation the network operates near criticality, producing large lin-

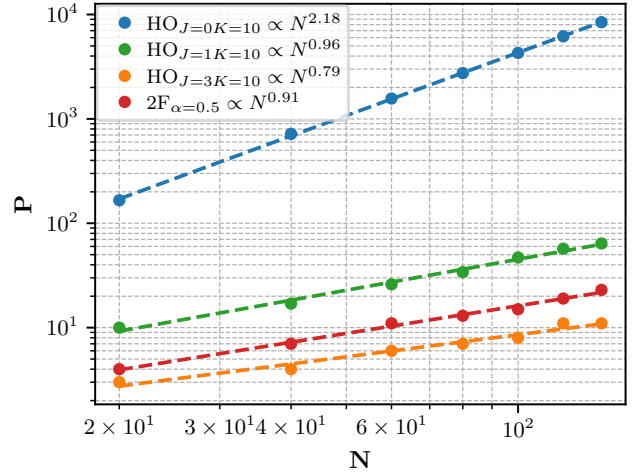


FIG. 7. Capacity scaling of the higher-order (HO) Kuramoto model at zero temperature (infinite  $\beta$ ). The system is setup in a random initial condition with 0.9% overlap to a target pattern and allowed to evolve after the dynamics of Eq. (6) for a long enough time for the system to converge. By calculating the absolute value of the overlap to the original pattern at the end and averaging over  $N_{\text{trials}} = 100$  we measure the highest number of patterns stored in a network of size  $N$  such that retrieval rate  $\chi \geq 0.95$ . The second-order Fourier (2F) model with  $\alpha = 0.5$  (red), higher-order Kuramoto model with  $J = 3$ ,  $K = 10$  (orange),  $J = 1$ ,  $K = 10$  (green),  $J = 0$ ,  $K = 10$  (blue). We observed improved scaling for models with larger ratio  $K/J$  over the second-order Fourier model. The best performance is achieved in the purely nonlinear case  $J = 0$ .

ear responses and short-lived yet information-rich transients before settling. Such behavior is advantageous in reservoir-computing where computation is performed by processing transient trajectories rather than by resting in a stable memory. In short,  $\beta J$  should be chosen in the bistable regime or at low  $C$  when continuous similarity search, energy-efficient state transitions, or transient signal processing is prioritized, whereas the single-well regime at high  $C$  remains preferable for rapid, stable pattern retention.

## CONCLUSIONS

We have introduced and analyzed a fourth-order Kuramoto model that elevates coupled-oscillator networks into the domain of dense associative memory. The work's primary theoretical advance is the demonstration that higher-order phase coupling can endow oscillatory networks with substantially enhanced memory storage capabilities, thereby showing that analog phase-based memories can achieve the high capacities previously known only in abstract  $p$ -spin Hopfield models [2, 3]. By augmenting the classical Kuramoto model with fourth-harmonic interaction terms, we constructed a system that can store a number of phase patterns growing super-linearly with network size while each pattern remains a stable dynamical

cal attractor. This represents a qualitative improvement over earlier oscillator networks (which were limited to  $O(1)$  patterns in the strict error-free sense) and even over the resonant second-harmonic model.

There are several advantages in using higher-order Kuramoto model. First, the advantage in capacity. When  $J = 0$  the  $r^4$  term dominates, crosstalk cancels at leading order and one obtains clear polynomial scaling as in the dense-memory Hopfield networks. Even for  $J > 0$  the quartic term increases the finite- $N$  factor: although the capacity scaling have similar slope, the pre-factors for  $J - K$  models are consistently higher than for pairwise Kuramoto model. Second, the advantage in controllable retrieval bifurcation. Setting  $K = 3J$  annihilates the  $r^4$  coefficient in (1) and marks a tricritical point. For  $K < 3J$  the memory onset is a super-critical pitchfork; for  $K > 3J$  it becomes a first-order transition with hysteresis and activation barriers  $\Delta F > 0, \Delta \mathcal{F} > 0$ . The quadratic model, by contrast, supports only a continuous transition. The ability to tune between "soft" and "latch-like" recall is valuable when one needs either easy accessibility (small cues) or maximum robustness (large basins separated by a barrier). At finite temperature it requires careful tuning of the coupling structure. In particular, moderate values of  $K$  alone are insufficient unless supported by a non-zero pairwise term  $J$ , which lowers the bifurcation threshold needed to destabilize the  $r = 0$  state. Alternatively, extremely strong higher-order coupling  $K \gg J$  can compensate and push the system into the latching regime without the need for pairwise interactions. While increasing  $K/J$  generally improves capacity, moderate ratios may offer practical advantages—such as controllability or reduced spurious attractor formation. Designing practical devices therefore requires calibrating nonlinear interaction strengths carefully, a consideration that parallels the stability-plasticity dilemma in neural memories and in condensed-matter systems with high-order interactions [6, 27]. Third, basin geometry and noise tolerance. In the bistable strip  $x_{\text{SN}}(K/J) < \beta J < x_{\text{P}}$  the free-energy barrier scales as  $\Delta F \sim K r^4$ , so the Kramer's escape time  $\tau_{\text{esc}} \sim \exp[\beta N \Delta F]$  grows exponentially with both  $K$  and  $N$ . Consequently, the quartic channel suppresses thermally activated errors orders of magnitude more effectively than the quadratic model whose barrier height is  $O(r^2)$ .

Besides performance, the  $J$ - $K$  model is closer to experimental reality. Photonic OPO networks, exciton-polariton lattices and superconducting Kerr-parametric oscillators already engineer effective four-body ring-exchange while inevitably retaining weak pairwise links; the mixed model therefore captures the operating regime of forthcoming hardware implementations. In summary, the quartic channel elevates asymptotic capacity from  $N/\log N$  to super linear, boosts the finite-size factor when  $J \neq 0$ , enables a tunable (continuous-to-explosive) retrieval onset that

is absent in the quadratic resonant model, and deepens basins enough to endow the network with superior noise immunity, all while matching the coupling structure realizable in modern oscillator platforms.

Our findings suggest several practical directions. The demonstrated capacity gains reinforce the promise of oscillator networks as analog content-addressable memories. With technologies such as coupled lasers and superconducting junction arrays already approaching the requisite nonlinearities, constructing a small-scale oscillator memory to test these predictions is within reach. Future theoretical work should explore higher values of  $p$ , heterogeneous natural-frequency distributions, and learning rules that adjust both pairwise and higher-order couplings in situ. Such studies would link the present model to modern Hopfield networks, equilibrium propagation, and analog gradient estimation. Moreover, the higher-order Kuramoto framework invites cross-disciplinary dialogue: from analog optimization to the interpretation of brain oscillatory patterns, underscoring its potential to inform both neuromorphic hardware design and the fundamental science of synchronization. In conclusion, embracing fourth-order interactions in oscillator networks significantly pushes the boundaries of analog associative memory, enabling a balance of continuous dynamics and dense storage that brings oscillatory Hopfield networks closer to practical realization.

## ACKNOWLEDGEMENTS

J.N. acknowledges the support from the EPSRC through PhD studentship EP/W524633/1. N.G.B. acknowledges the support from the HORIZON EIC Pathfinder Challenges project HEISINGBERG (grant 101114978), the Weizmann-UK Make Connection grant (grant 142568), and the EPSRC UK Multidisciplinary Centre for Neuromorphic Computing (grant UKRI982).

- 
- \* correspondence address: [N.G.Berloff@damtp.cam.ac.uk](mailto:N.G.Berloff@damtp.cam.ac.uk)
- [1] J. J. Hopfield, Neural networks and physical systems with emergent collective computational abilities, *Proceedings of the National Academy of Sciences* **79**, 2554 (1982).
  - [2] D. Krotov and J. J. Hopfield, Dense associative memory for pattern recognition, *Advances in Neural Information Processing Systems* **29** (2016).
  - [3] M. Demircigil, J. Heusel, M. Löwe, S. Uppang, and F. Vermet, On a model of associative memory with huge storage capacity, *Journal of Statistical Physics* **168**, 288 (2017), dOI: 10.1007/s10955-017-1808-4.
  - [4] A. Momeni, B. Rahmani, B. Scellier, L. G. Wright, P. L. McMahon, C. C. Wanjura, Y. Li, A. Skalli, N. G. Berloff, T. Onodera, *et al.*, Training of physical neural networks, arXiv preprint arXiv:2406.03372 (2024).

- [5] J. A. Acebrón, L. L. Bonilla, C. J. Pérez Vicente, F. Ritort, and R. Spigler, The kuramoto model: A simple paradigm for synchronization phenomena, *Reviews of Modern Physics* **77**, 137 (2005).
- [6] T. Nishikawa, F. C. Hoppensteadt, and Y.-C. Lai, Oscillatory associative memory network with perfect retrieval, *Physica D: Nonlinear Phenomena* **197**, 134 (2004).
- [7] P. S. Skardal and A. Arenas, Higher order interactions in complex networks of phase oscillators promote abrupt synchronization switching, *Communications Physics* **3**, 218 (2020).
- [8] L. V. Gambuzza, F. Di Patti, L. Gallo, S. Lepri, M. Romance, R. Criado, M. Frasca, V. Latora, and S. Boccaletti, Stability of synchronization in simplicial complexes, *Nature Communications* **12**, 1255 (2021).
- [9] N. Stroeve and N. G. Berloff, Discrete polynomial optimization with coherent networks of condensates and complex coupling switching, *Physical Review Letters* **126**, 050504 (2021).
- [10] Q. Wang, C. C. Wanjura, and F. Marquardt, Training coupled phase oscillators as a neuromorphic platform using equilibrium propagation, *Neuromorphic Computing and Engineering* **4**, 034014 (2024).
- [11] N. Stroeve and N. G. Berloff, Analog photonics computing for information processing, inference, and optimization, *Advanced Quantum Technologies* **6**, 2300055 (2023).
- [12] S. Kumar, H. Zhang, and Y.-P. Huang, Large-scale ising emulation with four body interaction and all-to-all connections, *Communications Physics* **3**, 108 (2020).
- [13] R. Salem, M. A. Foster, A. C. Turner, D. F. Geraghty, M. Lipson, and A. L. Gaeta, Signal regeneration using low-power four-wave mixing on silicon chip, *Nature Photonics* **2**, 35 (2008).
- [14] W. Min, S. Lu, M. Rueckel, G. R. Holtom, and X. S. Xie, Near-degenerate four-wave-mixing microscopy, *Nano Letters* **9**, 2423 (2009).
- [15] A. Rose, D. A. Powell, I. V. Shadrivov, D. R. Smith, and Y. S. Kivshar, Circular dichroism of four-wave mixing in nonlinear metamaterials, *Physical Review B* **88**, 195148 (2013).
- [16] J. E. Sharping, M. Fiorentino, P. Kumar, and R. S. Windeler, Optical parametric oscillator based on four-wave mixing in microstructure fiber, *Optics letters* **27**, 1675 (2002).
- [17] K. P. Kalinin and N. G. Berloff, Polaritonic network as a paradigm for dynamics of coupled oscillators, *Physical Review B* **100**, 245306 (2019).
- [18] T. Kanao and H. Goto, High-accuracy ising machine using kerr-nonlinear parametric oscillators with local four-body interactions, *npj Quantum Information* **7**, 18 (2021).
- [19] M. K. Bashar and N. Shukla, Designing ising machines with higher order spin interactions and their application in solving combinatorial optimization, *Scientific Reports* **13**, 9558 (2023).
- [20] M. K. Bashar, Z. Lin, and N. Shukla, Oscillator-inspired dynamical systems to solve boolean satisfiability, *IEEE Journal on Exploratory Solid-State Computational Devices and Circuits* **9**, 12 (2023).
- [21] G. Pedretti, F. Böhm, T. Bhattacharya, A. Heitmann, X. Zhang, M. Hizzani, G. Hutchinson, D. Kwon, J. Moon, E. Valiante, *et al.*, Solving boolean satisfiability problems with resistive content addressable memories, *npj Unconventional Computing* **2**, 7 (2025).
- [22] T. Makinwa, K. Inaba, T. Inagaki, Y. Yamada, T. Leleu, T. Honjo, T. Ikuta, K. Enbutsu, T. Umeki, R. Kasahara, *et al.*, Experimental observation of chimera states in spiking neural networks based on degenerate optical parametric oscillators, *Communications Physics* **6**, 121 (2023).
- [23] L. Martins, A. S. Jenkins, J. Borme, J. Ventura, P. P. Freitas, and R. Ferreira, Second harmonic injection locking of coupled spin torque vortex oscillators with an individual phase access, *Communications Physics* **6**, 72 (2023).
- [24] T. Böhnert, Y. Rezaeiyan, M. Claro, L. Benetti, A. Jenkins, H. Farkhani, F. Moradi, and R. Ferreira, Weighted spin torque nano-oscillator system for neuromorphic computing, *Communications Engineering* **2**, 65 (2023).
- [25] W. A. Borders, A. Z. Pervaiz, S. Fukami, K. Y. Camsari, H. Ohno, and S. Datta, Integer factorization using stochastic magnetic tunnel junctions, *Nature* **573**, 390 (2019).
- [26] V. H. González, A. Litvinenko, A. Kumar, R. Khymyn, and J. Åkerman, Spintronic devices as next-generation computation accelerators, *Current Opinion in Solid State and Materials Science* **31**, 101173 (2024).
- [27] R. G. Melko and A. W. Sandvik, Stochastic series expansion algorithm for the  $s=1/2$  xy model with four-site ring exchange, *Physical Review E* **72**, 026702 (2005).
- [28] I. S. Aranson and L. Kramer, The world of the complex ginzburg-landau equation, *Reviews of Modern Physics* **74**, 99 (2002).
- [29] L. Angelani and G. Ruocco, Phase transitions and topology in  $2+1$  k xy mean-field models, *Physical Review E—Statistical, Nonlinear, and Soft Matter Physics* **76**, 051119 (2007).
- [30] Y. Zhang, M. Lucas, and F. Battiston, Higher-order interactions shape collective dynamics differently in hypergraphs and simplicial complexes, *Nature Communications* **14**, 1605 (2023).
- [31] A. Mallick, M. K. Bashar, Z. Lin, and N. Shukla, Computational models based on synchronized oscillators for solving combinatorial optimization problems, *Physical Review Applied* **17**, 064064 (2022).
- [32] S. Nikhar, S. Kannan, N. A. Aadit, S. Chowdhury, and K. Y. Camsari, All-to-all reconfigurability with sparse and higher-order ising machines, *Nature Communications* **15**, 8977 (2024).
- [33] E. Ott and T. M. Antonsen, Low dimensional behavior of large systems of globally coupled oscillators, *Chaos: An Interdisciplinary Journal of Nonlinear Science* **18** (2008).
- [34] F. Parastesh, M. Mehrabbeik, K. Rajagopal, S. Jafari, and M. Perc, Synchronization in hindmarsh-rose neurons subject to higher-order interactions, *Chaos: An Interdisciplinary Journal of Nonlinear Science* **32** (2022).
- [35] N. Wildberger and D. Rubine, A hyper-catalan series solution to polynomial equations, and the geode, *The American Mathematical Monthly* **132**, 383 (2025).
- [36] H. A. Kramers, Brownian motion in a field of force and the diffusion model of chemical reactions, *Physica* **7**, 284 (1940).
- [37] R. B. Griffiths, C.-Y. Weng, and J. S. Langer, Relaxation times for metastable states in the mean-field model of a ferromagnet, *Physical Review* **149**, 301 (1966).